Harsha S. Bhat[1]
Department of Earth Sciences,
University of Southern California & Graduate
Aerospace Laboratories,
California Institute of Technology,
Pasadena, CA, 91125
e-mail: bhat@ipgp.fr

Ares J. Rosakis
Graduate Aerospace Laboratories,
California Institute of Technology,
Pasadena, CA, 91125
e-mail: arosakis@caltech.edu

Charles G. Sammis
Department of Earth Sciences,
University of Southern California,
Los Angeles, CA, 90089
e-mail: sammis@usc.edu

A Micromechanics Based Constitutive Model for Brittle Failure at High Strain Rates

*The micromechanical damage mechanics formulated by Ashby and Sammis, 1990, "The Damage Mechanics of Brittle Solids in Compression," Pure Appl. Geophys., **133**(3), pp. 489–521, and generalized by Deshpande and Evans 2008, "Inelastic Deformation and Energy Dissipation in Ceramics: A Mechanism-Based Constitutive Model," J. Mech. Phys. Solids, **56**(10), pp. 3077–3100. has been extended to allow for a more generalized stress state and to incorporate an experimentally motivated new crack growth (damage evolution) law that is valid over a wide range of loading rates. This law is sensitive to both the crack tip stress field and its time derivative. Incorporating this feature produces additional strain-rate sensitivity in the constitutive response. The model is also experimentally verified by predicting the failure strength of Dionysus-Pentelicon marble over strain rates ranging from $\sim 10^{-6}$ to $10^3 \mathrm{s}^{-1}$. Model parameters determined from quasistatic experiments were used to predict the failure strength at higher loading rates. Agreement with experimental results was excellent.* [DOI: 10.1115/1.4005897]

1 Introduction

The deformation of brittle materials like rocks, concrete or ceramics is known to be sensitive to internal fractures, which are commonly characterized as damage. Tensile cracks induced by grain-boundary sliding are a major source of inelastic deformation in these materials. The effects of damage are especially important in phenomena that involve high levels of stress, and a wide rage of strain-rates, such as earthquakes, underground explosions, and meteorite impacts. At the high loading rates that typify these phenomena the evolution of damage is sensitive not only to the initial damage, but also to the rate at which the load is applied.

Behavior typical of such materials includes : (a) nonlinear stress-strain relations (b) a failure mode that depends on confining pressure (mean stress) ranging from axial splitting to shear localization to pseudoplasticity as confining pressure increases (c) decrease of elastic moduli with increasing damage, and (d) permanent residual strains associated with micro-crack opening and sliding.

Modeling the constitutive response of these materials requires taking into account the mechanics of micro-cracks and their overall response to applied loading. One approach is to appeal to averaging schemes that determine elastic constants like the self-consistent schemes [1]. Another approach is to calculate the continuum response of micro-crack filled brittle materials from the Gibbs free energy function [2–9]. Although these models account for the physical mechanisms associated with cracks, they lack a physical crack growth law and hence a physical representation of the evolving damage. A common law used here is the Charles law [10] where the crack speed is proportional to some power of the crack tip stress intensity factor. Unfortunately such laws are valid for sub-critical crack growth (see Ref. [11] for a review) but are clearly not valid in the dynamic range. Thus any attempt to develop a model valid over a wide range of loading rates requires a more physical (crack growth) law. Rate effects are particularly important at high loading rates where crack growth lags the loading. We note here that [9] have attempted to model crack growth in this loading regime by solving for a crack-speed

that ensures that the dynamic stress intensity factor of the crack always equals the fracture toughness. However their work did not account for the fact that the fracture toughness of the material is itself sensitive to loading rate.

The micromechanical damage mechanics formulated by Ashby and Sammis [12] models the nucleation, growth, and interaction of a mono-sized distribution of cracks having a fixed orientation. We use this model as a template to develop our micromechanical damage model. The main features/assumptions of their formulation were:

(1) The starter cracks all have the same radius a and are all oriented at the same angle Ψ, to be specified later, relative to the axis of principal compression σ_1. In the dynamic problem this changes with time and so do populations of activated cracks. There are N_V such starter flaws per unit volume. Sliding on the starter cracks is inhibited by Coulomb friction characterized by coefficient f.

(2) All additional crack damage is in the form of tensile "wing cracks" that nucleate at the tips of the starter flaws and grow parallel to σ_1 axis. They open in the direction of the least compressive principal stress σ_3.

(3) The stress at which the wing cracks nucleate is taken from results in the literature and may be expressed as

$$\sigma_{1c} = \left(\frac{\sqrt{1+f^2}+f}{\sqrt{1+f^2}-f} \right) \sigma_3 - \left(\frac{\sqrt{3}}{\sqrt{1+f^2}-f} \right) \frac{K_{IC}}{\sqrt{\pi a}} \quad (1)$$

where K_{IC} is the fracture toughness.

(4) The stress intensity factor K_I at the tips of the growing wing cracks (of length l) is approximated as that at the tip of a tensile crack of radius $l + \alpha a$ that is loaded by a point force at its center. The point force is taken as the σ_3 component of force generated by frictional sliding on the starter flaw. The geometrical factor α is the projection of the starter flaw on the σ_1 axis. This approximation was tested against the numerical solution and found to be poor for small l but asymptotically better as l increases. An adjustable parameter β was introduced to improve the fit of the approximate K_I to the numerical calculations of K_I at small values of l.

(5) The failure stress $\sigma_1^*(\sigma_3)$ is defined as the maximum value of σ_1 versus l curve at constant σ_3.

There are thus four crack related parameters in the model:

(1) $\alpha = \cos\Psi$ where Ψ is the angle between the starter crack and the σ_1 axis.
(2) β adjusted to make the approximate expression for K_I agree with the full numerical simulation when the wing cracks are short.
(3) $a =$ radius of the starter flaws. It is found by fitting the nucleation equation above to the observed onset of nonlinearity in the stress strain curve or the onset of acoustic emissions.
(4) $N_V =$ number of favorably oriented (active) starter flaws per unit volume. It is found by fitting the uniaxial strength.

Despite these apparently crude approximations, [12] found that this approximate model gave a very good fit to the failure surfaces, $\sigma_1^*(\sigma_3)$, of a wide range of rocks for reasonable values of a (approximately the grain size) and N_V. It was later shown by [13] that the inclusion of size distribution of cracks and allowance for multiple crack orientations did not significantly effect the failure strength predicted by the model. We thus retain the single-crack single-orientation assumption of [2,12].

The model is based on the growth and interaction of tensile "wing cracks" nucleated at the tips of an initial distribution of micro-cracks. It incorporates results from many studies of mode I wing cracks nucleated and driven by mode II sliding (for example see [3,4,14–16] and references therein). By approximating the interaction between growing wing cracks [12] found a positive feedback that led to mechanical instability and failure. They demonstrated that their model gave an adequate description of the failure envelope (σ_1 versus σ_3 at failure) for a wide range of rocks loaded in triaxial compression ($\sigma_1 < \sigma_2 = \sigma_3$, where compression is taken as negative). However since quasi-static crack growth was assumed (the stress intensity factor is always at its critical value) their formulation does not include effects of loading rate. Ref. [2] introduced Charles crack growth law [10] into Ref. [12] in order to simulate impact loading of ceramic armor plates. However, as described above, such laws are typically used to describe stress corrosion and do not contain the known physics of dynamic crack growth. In this paper, we extend the damage mechanics formulation in [2,12] by incorporating theoretical and experimental dynamic crack growth laws that have been shown to be valid over a wide range of loading rates. We then compare the model predictions with uniaxial experiments in marble over a wide range of loading rates ($\dot{\varepsilon} \sim 10^{-6}$ to $10^3 s^{-1}$).

2 Development of the Constitutive Model

In most brittle materials, micro-crack nucleation, growth and coalescence is driven by local sliding at micro-cracks or grain boundaries [17] as shown schematically in Fig. (1(a)). This micro-crack physics produces inelastic dilatancy, modulus reduction and strain-rate sensitivity of failure strength. Thus any realistic constitutive model of brittle materials should take into account the micromechanics of fracture.

2.1 Continuum Constitutive Model From Micro-Scale Deformations Based On J. R. Rice, 1975. Following the framework laid out by Refs. [18,19] we use an energy-based approach to determine the constitutive relationship of the damaged solid. As in Ref. [19], let S denote the current damaged state of the material in the sense that variations in stress at constant S induce a purely elastic response. Then the stress-strain relationship and the compliance tensor in terms of a Gibbs free energy function, W, under isothermal conditions are given by

$$\varepsilon_{ij} = \frac{\partial W(\boldsymbol{\sigma}, S)}{\partial \sigma_{ij}}; \quad M_{ijkl} = \frac{\partial^2 [W(\boldsymbol{\sigma}, S)]}{\partial \sigma_{ij} \partial \sigma_{kl}} \quad (2)$$

where W is symmetrized in the components of $\boldsymbol{\sigma}$ (notations in bold represent tensorial quantities).

Let dW denote the change in the free energy function when the solid undergoes deformation that takes it from the state S to $S + dS$ at constant σ_{ij}. Therefore the inelastic strain associated with dW is given by
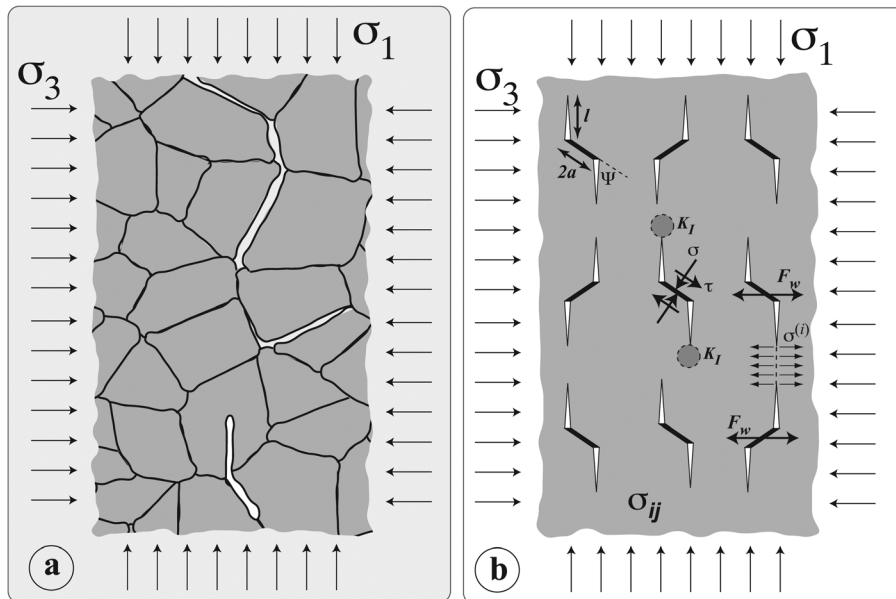

Fig. 1 Geometry in the [12] micromechanical damage mechanics model. Sliding on an array of penny-shaped cracks having volume density of N_V and radius a produces a wedging force F_w that drives tensile wing cracks to open in the direction of the smallest principal stress σ_3 and propagate parallel to the largest principal stress σ_1. Growth of wing cracks is enhanced by σ_1, retarded by σ_3, and enhanced by a global interaction that produces a mean tensile stress σ_3^i. The positive feedback provided by this tensile interaction stress leads to a run-away growth of the wing cracks and ultimate macroscopic failure.

$$d\varepsilon_{ij} = \frac{\partial(dW)}{\partial\sigma_{ij}} \qquad (3)$$

Let Γ be the locus of all crack fronts in the damaged solid and let ds be a function of position along Γ describing the amount of local advance of the micro-cracks. Then the change in the free energy function is given by

$$dW = \int_{\Gamma}\{[G(\boldsymbol{\sigma},S) - 2\gamma_s]ds\}d\Gamma \qquad (4)$$

where G is the elastic energy release rate and γ_s is the surface energy. The inelastic strain in now given by

$$d\varepsilon_{ij} = \frac{\partial}{\partial\sigma_{ij}}\left[\int\!\!\int_{\Gamma} G(\boldsymbol{\sigma},S)ds\ d\Gamma\right] \equiv \frac{\partial(\Delta W)}{\partial\sigma_{ij}} \qquad (5)$$

From linear elastic fracture mechanics, the energy release rate, G is related to the stress intensity factor by

$$G(\boldsymbol{\sigma},S) = \frac{1-\nu^2}{E}\left[K_I^2(\boldsymbol{\sigma},S) + K_{II}^2(\boldsymbol{\sigma},S) + \frac{K_{III}^2(\boldsymbol{\sigma},S)}{(1-\nu)}\right] \qquad (6)$$

The above expression is valid as long as the crack has continuously turning tangent planes, i.e., without sudden kinks, forks or branches. Thus,

$$\Delta W(\boldsymbol{\sigma},S) = \frac{1-\nu^2}{E}\int_{\Gamma}\left[K_I^2(\boldsymbol{\sigma},S) + K_{II}^2(\boldsymbol{\sigma},S) + \frac{K_{III}^2(\boldsymbol{\sigma},S)}{1-\nu}\right]ds\ d\Gamma \qquad (7)$$

where ν is the Poisson's ratio and E is the Young's modulus.

Therefore the Gibbs free energy can be written as the sum of the elastic contribution and the inelastic one due to the presence of micro-cracks.

$$W(\boldsymbol{\sigma},S) = W^e(\boldsymbol{\sigma}) + \frac{1-\nu^2}{E}\int_{\Gamma}\left[K_I^2(\boldsymbol{\sigma},S) + K_{II}^2(\boldsymbol{\sigma},S) \right.$$
$$\left. + \frac{K_{III}^2(\boldsymbol{\sigma},S)}{(1-\nu)}\right]ds\ d\Gamma \qquad (8)$$

where W^e is the elastic strain energy. The stress-strain relation and the compliance tensor are then given by Eq. (2). The precise definition of S will be laid out later.

2.2 Evaluation of the Stress Intensity Factors. The purpose of this work is to use the framework describe above and evaluate the Gibbs free energy, Eq. (8), and hence the stress-strain relationship and the compliance tensor, for a particular micro-crack model. In this work, following Refs. [12] and [2], we begin by considering an isotropic elastic solid that contains an array of penny shaped cracks all of radius a (micro-cracks or grain boundaries) and all aligned at an angle Ψ to the largest (most negative) remote compressive stress σ_1 (Fig. 1(b)). By aligning the cracks with respect to the maximum principal stress, we only take into account cracks that are optimally oriented, the precise criteria will be discussed later, for growth. We also assume that the population of cracks that exist prior to loading has the volume density, N_v, and remains fixed during loading. *No new cracks nucleate during loading.* The size and density of these initial flaws are characterized by initial damage defined through a scalar variable as

$$D_o = \frac{4}{3}\pi N_V(\alpha a)^3 \qquad (9)$$

where αa is the projection of the crack radius in a vertical plane parallel to the direction of σ_1, $\alpha = \cos\Psi$.

Refs. [2,12,13] calculate the shear (τ) and normal (σ) stresses on each penny crack from the remote compressive stress field.

$$\tau = \left(\frac{\sigma_3 - \sigma_1}{2}\right)\sin 2\Psi$$
$$\sigma = \left(\frac{\sigma_3 + \sigma_1}{2}\right) + \left(\frac{\sigma_3 - \sigma_1}{2}\right)\cos 2\Psi \qquad (10)$$

For ease of numerical implementation, Ref. [2] rewrote these equations in terms of stress invariants by making the assumption that $\sigma_2 = (\sigma_3 + \sigma_1)/2$. We remove this restriction on the intermediate principal stress by assuming that the shear stress, τ, is represented by the second invariant of the deviatoric stress tensor and the normal stress, σ, is calculated from the first invariant of the stress tensor, i.e.,

$$\tau = \sqrt{\frac{1}{2}S_{ij}S_{ij}} \quad \text{and} \quad \sigma = \frac{\sigma_{kk}}{3} \qquad (11)$$

where $S_{ij} = \sigma_{ij} - \sigma\delta_{ij}$ and δ_{ij} is the Kronecker δ. This operation is analogous to Ref. [20] where the Mohr-Coulomb failure criterion was extended to a generalized stress state. Sliding on the cracks is controlled by a coefficient of friction f. We only consider flaws that are optimally oriented from a Coulomb friction perspective. This implies $\Psi = \tan^{-1}(1/f)$. Note that Eqs. (10) and (11) coincide when $\sigma_2 = (\sigma_3 + \sigma_1)/2$ and $f = 1.0$. However, typical values of f in brittle solids are closer to $f = 0.6$.

As in Ref. [2], we delineate three deformation regimes for the micro-cracked solid based on the remote loading state. In *Regime I*, the remote loading is compressive and is not large enough to overcome the frictional resistance on the penny shaped cracks. The solid thus behaves like an isotropic linear elastic solid. In *Regime II* the frictional resistance on the micro-cracks is overcome by the remote compressive load leading to the nucleation and growth of wing-cracks. In *Regime III* the remote loading stresses turn tensile leading to the opening of both the penny crack and wing-cracks. The criteria for transition between regimes will be laid out later in the text.

Regime II: Following [2,12] we evaluate the Mode-I stress intensity factor, K_I, at the tip of the wing-cracks (of length l) that emanate from the periphery of the sliding penny cracks. Note that any Mode-II and Mode-III contributions are relevant only during the nucleation phase of the wing cracks and are hence ignored. We also neglect any opening of the penny crack induced by the tensile wing cracks (see Ref. [16]). Since the wing cracks are aligned with respect to the maximum principal stress, σ_1, any rotation in the principal stress field would also implicitly result in the rotation of a wing crack so that it always follows the principal of local symmetry.

The Mode-I stress intensity factor has three contributions: (1) Sliding on the penny cracks leads to a wedging force, F_w, on the wing-cracks. This wedging force is simply the component of the sliding force resolved normal to the direction of the maximum principal stress, i.e., $F_w = (\tau + f\sigma)\pi a^2\sin\Psi$. (2) The remote confining stress, characterized by σ, tends to close the wing-cracks and, (3) the wedging force, F_w, creates tension $\sigma^{(i)}$ on the unbroken ligaments between neighboring wing-cracks (see Fig. 1) thus producing a global interaction between micro-cracks. Therefore the Mode-I stress intensity factor in this regime, K_I^{R-II}, is given by

$$K_I^{R-II} = \frac{(\tau + f\sigma)\pi a^2\sin\Psi}{[\pi(l+\beta a)]^{3/2}} + \frac{2}{\pi}\left(\sigma + \sigma^{(i)}\right)\sqrt{\pi l} \qquad (12)$$

where

$$\sigma^{(i)} = \frac{(\tau + f\sigma)\pi a^2\sin\Psi}{A_{\text{crack}} - \pi(l+\alpha a)^2}; \quad A_{\text{crack}} = \pi^{1/3}\left(\frac{3}{4N_v}\right)^{2/3}$$

Here, A_{crack} is the average area occupied per crack, $\pi(l+\alpha a)^2$ is the total crack area projected parallel to σ_1 and $\sin\Psi = \sqrt{1-\alpha^2}$. The factor $\beta(=0.1)$ was introduced by Ref. [12] to give a limiting value of K_I when the wing-crack length, l, vanished to zero.

We now define a scalar damage parameter that accounts for the current size of each crack and the volume density of such cracks. As in Eq. (9), we define

$$D = \frac{4}{3}\pi N_V(l+\alpha a)^3 \tag{13}$$

This scalar damage parameter represents the state of the microstructure, S, as described by Ref. [19].

By rewriting Eq. (12) in terms D and D_0 we obtain

$$K_I^{R-II}(\boldsymbol{\sigma},D) = \sqrt{\pi a}[A(D)\sigma + B(D)\tau] \tag{14}$$

$$A(D) = fc_1(D) + (1+f)c_2(D)c_3(D)$$
$$B(D) = c_1(D) + c_2(D)c_3(D) \tag{15}$$

and

$$c_1(D) = \frac{\sqrt{1-\alpha^2}}{\pi\alpha^{3/2}[(D/D_0)^{1/3}-1+\beta/\alpha]^{3/2}}$$

$$c_2(D) = \left(\frac{\sqrt{1-\alpha^2}}{\alpha^2}\right)\left(\frac{D_0^{2/3}}{1-D^{2/3}}\right)$$

$$c_3(D) = \frac{2\sqrt{\alpha}}{\pi}[(D/D_0)^{1/3}-1]^{1/2} \tag{16}$$

Since Eq. (14) is now written in terms of D and D_0, which account of the current size of each crack and the volume density of such cracks, it represents a measure of the stress intensity factor for all cracks of size $l+\alpha a$ in a unit representative volume. This step thus effectively homogenizes K_I. The above expressions for K_I also puts a limit on the maximum value of D. As D approaches 1, K_I becomes unbounded representing the limit when neighboring wing-cracks coalesce.

Regime III: As in Ref. [2], we also allow for the possibility of the overall remote loading stress turning tensile. In this case, following [1,5,21] we write the Mode-I stress intensity factor, K_I^{R-III}, as a quadratic function of stresses,

$$K_I^{R-III}(\boldsymbol{\sigma},D) = \sqrt{\pi a}[C^2(D)\sigma^2 + E^2(D)\tau^2]^{1/2} \tag{17}$$

where $C(D)$, $E(D)$ will be related to $A(D)$, $B(D)$ by ensuring that the elastic strains match when transitioning from a remote compressive stress state to a remote tensile one.

2.3 Constitutive Relationship. We start with the evaluation of the Gibbs free energy function in *Regime's I, II and III* using the stress intensity factors calculated in the previous section and eqn. (8). We then differentiate the Gibbs free energy function as shown in eqn. (2) to obtain the stress-strain relationship and the compliance and modulus tensors. Thus,

Regime I: The stress-strain relationship is given by

$$\sigma_{ij} = 2\mu\varepsilon_{ij} - \frac{2\mu v}{(1-2v)}\varepsilon\delta_{ij} \tag{18}$$

Regime II: The Gibbs free energy function is given by

$$W(\boldsymbol{\sigma},D) = W^e(\boldsymbol{\sigma}) + \frac{1}{4\mu}[A_1\sigma + B_1\tau]^2 \tag{19}$$

In performing the integral in Eq. (8), following Ref. [2], we assume A and B to be functions of only l/a (and not l and a separately), and thus treating them as constants. This is only approximately true but this assumption renders an analytical closed form for W. Differentiating the above expression with respect to stress (see Eq. (2)) we obtain the stress-strain relation,

$$\varepsilon_{ij}(\boldsymbol{\sigma},D) = \frac{1}{2\mu}\left\{\left(1+\frac{A_1B_1\sigma}{2\tau}+\frac{B_1^2}{2}\right)\sigma_{ij}\right.$$
$$\left. -\left(\frac{3\nu}{(1+\nu)}+\frac{A_1B_1\sigma}{2\tau}-\frac{A_1^2}{3}+\frac{B_1^2}{2}\right)\sigma\delta_{ij}+\left(\frac{A_1B_1}{3}\right)\tau\delta_{ij}\right\} \tag{20}$$

Differentiating the Gibbs free energy function twice with respect to stress (see Eq. (2)) we obtain the compliance tensor

$$M_{ijkl}(\boldsymbol{\sigma},D) = \frac{1}{2\mu}\left\{\left(\frac{1}{2}+\frac{B_1^2}{4}+\frac{A_1B_1\sigma}{4\tau}\right)(\delta_{ki}\delta_{lj}+\delta_{li}\delta_{kj})\right.$$
$$-\left(\frac{\nu}{(1+\nu)}+\frac{B_1^2}{6}-\frac{A_1^2}{9}+\frac{A_1B_1\sigma}{2\tau}+\frac{A_1B_1\sigma^3}{2\tau^3}\right)\delta_{ij}\delta_{kl}$$
$$+\left(\frac{A_1B_1}{6}+\frac{A_1B_1\sigma^2}{4\tau^2}\right)(\hat{\sigma}_{ij}\delta_{kl}+\delta_{ij}\hat{\sigma}_{kl})$$
$$\left.-\left(\frac{A_1B_1\sigma}{4\tau}\right)\hat{\sigma}_{ij}\hat{\sigma}_{kl}\right\} \tag{21}$$

where $\hat{\sigma}_{ij} = \sigma_{ij}/\tau$ and

$$A_1 = A\sqrt{\frac{\pi D_0}{\alpha^3(1+\nu)}} \quad B_1 = B\sqrt{\frac{\pi D_0}{\alpha^3(1+\nu)}} \tag{22}$$

Equation (19) can be recast in terms of conjugate strains, ε and γ, where $\varepsilon = \varepsilon_{kk}$, $\gamma = \sqrt{2e_{ij}e_{ji}}$ and $e_{ij} = \varepsilon_{ij} - \varepsilon_{ij} - \varepsilon\delta_{ij}/3$. Differentiating the modified Gibbs free energy function with respect to strain we obtain

$$\sigma_{ij}(\boldsymbol{\varepsilon},D) = 2\mu\left\{\left(1+\frac{2\bar{A}_1\bar{B}_1\varepsilon}{\gamma}+2\bar{B}_1^2\right)\varepsilon_{ij}\right.$$
$$\left.+\left(\frac{\nu}{(1-2\nu)}-\frac{2\bar{A}_1\bar{B}_1\varepsilon}{3\gamma}-\frac{2\bar{B}_1^2}{3}+\bar{A}_1^2\right)\varepsilon\delta_{ij}+(\bar{A}_1\bar{B}_1)\gamma\delta_{ij}\right\} \tag{23}$$

The damage dependent constants $\bar{A}_1$ and $\bar{B}_1$ are given by

$$\bar{A}_1(D) = \frac{1}{2}(A_1a_1 + B_1b_1)$$
$$\bar{B}_1(D) = \frac{1}{2}(A_1a_1 + B_1b_2) \tag{24}$$

where

$$a_1 = \frac{1}{\Gamma}\left(1+\frac{B_1^2}{2}\right) \quad b_1 = -\frac{1}{\Gamma}\left(\frac{A_1B_1}{2}\right)$$

$$b_2 = \frac{1}{\Gamma}\left[\frac{A_1^2}{2}+\frac{3(1-2\nu)}{2(1+\nu)}\right]$$

$$\Gamma = \left[\frac{3(1-2\nu)}{2(1+\nu)}+\frac{3(1-2\nu)B_1^2}{4(1+\nu)}+\frac{A_1^2}{2}\right]$$

The modulus tensor is obtained by differentiating Eq. (23) with respect to stress,

$$C_{ijkl}(\boldsymbol{\varepsilon}, D) = 2\mu\left\{\left(\frac{1}{2} + \bar{B}_1^2 + \frac{\bar{A}_1\bar{B}_1\varepsilon}{\gamma}\right)(\delta_{ki}\delta_{lj} + \delta_{li}\delta_{kj})\right.$$
$$+ \left(\frac{\nu}{(1-2\nu)} - \frac{2\bar{B}_1^2}{3} + \bar{A}_1^2 - \frac{2\bar{A}_1\bar{B}_1\varepsilon}{\gamma} - \frac{4\bar{A}_1\bar{B}_1\varepsilon^3}{9\gamma^3}\right)\delta_{ij}\delta_{kl}$$
$$+ \left(\frac{2\bar{A}_1\bar{B}_1}{\gamma} + \frac{4\bar{A}_1\bar{B}_1\varepsilon^2}{3\gamma^2}\right)(\hat{\varepsilon}_{ij}\delta_{kl} + \delta_{ij}\hat{\varepsilon}_{kl})$$
$$\left. - \left(\frac{4\bar{A}_1\bar{B}_1\varepsilon}{\gamma}\right)\hat{\varepsilon}_{ij}\hat{\varepsilon}_{kl}\right\} \tag{25}$$

where $\hat{\varepsilon}_{ij} = \varepsilon_{ij}/\gamma$.

Regime III: The Gibbs free energy function is given by

$$W(\boldsymbol{\sigma}, D) = W^e(\boldsymbol{\sigma}) + \frac{1}{4\mu}[C_1^2\sigma^2 + E_1^2\tau^2] \tag{26}$$

Differentiating the above expression with respect to stress (see Eq. (2)), we obtain the stress-strain relation

$$\varepsilon_{ij}(\boldsymbol{\sigma}, D) = \frac{1}{2\mu}\left\{\left(1 + \frac{E_1^2}{2}\right)\sigma_{ij} - \left(\frac{3\nu}{(1+\nu)} + \frac{E_1^2}{2} - \frac{C_1^2}{3}\right)\sigma\delta_{ij}\right\} \tag{27}$$

Differentiating the Gibbs free energy function twice with respect to stress (see Eq. (2)) we obtain the compliance tensor

$$M_{ijkl}(\boldsymbol{\sigma}, D) = \frac{1}{2\mu}\left\{\left(1 + \frac{E_1^2}{4}\right)(\delta_{ki}\delta_{lj} + \delta_{li}\delta_{kj})\right.$$
$$\left. - \left(\frac{\nu}{(1+\nu)} + \frac{E_1^2}{6} - \frac{C_1^2}{9}\right)\delta_{ij}\delta_{kl}\right\} \tag{28}$$

where

$$C_1 = C\sqrt{\frac{\pi D_0}{\alpha^3(1+\nu)}} \quad E_1 = E\sqrt{\frac{\pi D_0}{\alpha^3(1+\nu)}} \tag{29}$$

Equation (26) can be recast in terms of conjugate strains, ε and γ, where $\varepsilon = \varepsilon_{kk}$, $\gamma = \sqrt{2e_{ij}e_{ji}}$ and $e_{ij} = \varepsilon_{ij} - \varepsilon\delta_{ij}/3$. Differentiating the modified Gibbs free energy function with respect to strain we obtain

$$\sigma_{ij}(\boldsymbol{\varepsilon}, D) = 2\mu\left\{\left(1 + 2\bar{E}_1^2\right)\varepsilon_{ij} + \left(\frac{\nu}{(1-2\nu)} - \frac{2\bar{E}_1^2}{3} + \bar{C}_1^2\right)\varepsilon\delta_{ij}\right\} \tag{30}$$

where $\varepsilon = \varepsilon_{kk}$, $\gamma = \sqrt{2e_{ij}e_{ji}}$ and $e_{ij} = \varepsilon_{ij} - \varepsilon\delta_{ij}/3$. The damage dependent constants $\bar{C}_1$ and $\bar{E}_1$ are given by

$$\bar{C}_1(D) = \frac{C_1}{\left\{\frac{3(1-2\nu)}{(1+\nu)} + C_1^2\right\}} \quad \bar{E}_1(D) = \frac{E_1}{\{2 + E_1^2\}} \tag{31}$$

The modulus tensor is obtained by differentiating Eq. (30) with respect to strain to obtain

$$C_{ijkl}(\boldsymbol{\varepsilon}, D) = 2\mu\left\{\left(\frac{1}{2} + \bar{E}_1^2\right)(\delta_{ki}\delta_{lj} + \delta_{li}\delta_{kj})\right.$$
$$\left. + \left(\frac{\nu}{(1-2\nu)} - \frac{2\bar{E}_1^2}{3} + \bar{C}_1^2\right)\delta_{ij}\delta_{kl}\right\} \tag{32}$$

As in Ref. [2], ensuring the work conjugate strains, ε and γ, are continuous when transitioning from *Regime II* to *Regime III* gives

$$E^2 = \frac{B^2C^2}{C^2 - A^2} \tag{33}$$

C is obtained by matching the stress intensity factors in *Regime II* and *Regime III* under pure hydrostatic tension, which gives

$$C = A + \Omega\sqrt{\alpha\left(\frac{D}{D_0}\right)^{1/3}} \tag{34}$$

where Ω is a crack shape factor and is set to be 2.0.

The criteria for transition between regimes can be obtained as follows. In *Regime I* the stresses are not large enough to allow for sliding or opening of the micro-cracks. This implies K_I^{R-II} (or equivalently K_I^{R-III} since C and E are related to A and B) is negative.

Therefore, in *Regime I* (from Eq. (14))

$$A\sigma + B\tau \leq 0 \tag{35}$$

Transition criteria from *Regime II* to *Regime III* are obtained again by ensuring continuity of conjugate strains, ε and γ.

Thus, in *Regime II*,

$$A\sigma + B\tau > 0 \quad \text{and} \quad (A^2 - C^2)\sigma + AB\tau < 0 \tag{36}$$

And finally in *Regime III*,

$$A\sigma + B\tau > 0 \quad \text{and} \quad (A^2 - C^2)\sigma + AB\tau > 0 \tag{37}$$

2.4 Damage Evolution Law. To complete the constitutive model described above, we need to prescribe an evolution law to the scalar damage parameter, D. Differentiating D with respect to time we obtain

$$\frac{dD}{dt} = \left(\frac{3D^{2/3}D_0^{1/3}}{\alpha a}\right)\frac{dl}{dt} \tag{38}$$

where $dl/dt \equiv v$ is the instantaneous wing-crack tip speed. This is a geometric relation connecting the wing crack tip speed with the evolution of the damage parameter D. Completing this process will now necessitate the introduction of additional physics relating dl/dt to local stress conditions at the vicinity of the micro-cracks. This is typically done through the notion of a micro-crack stress intensity factor and its critical values (toughness) for both initiation and growth.

If the history of the crack-tip motion is specified, then the surrounding mechanical fields in an elastic body can be obtained using linear elastic continuum mechanics, as long as the configuration of the body and the details of the loading are specified. However, since the motion of crack-tip is totally controlled by the deformation state inside the surrounding material, the motion of the crack-tip should not be specified a priori. Due to the fact that the constitutive equation for the material does not include the possibility of material separation, we need a mathematical statement of a crack growth criterion to be added into the governing equations. Such a criterion must be stated as a physical postulate on material failure at the same level as the kinematical theorems governing deformation, momentum balance principles, as well as the constitutive relation describing material response.

Thus, to properly solve this problem, one needs to understand the state of stress around a crack-tip (both stationary and propagating) under various loading conditions. These values then need to be compared with experimentally determined fracture toughness of the material, under similar conditions, to develop crack initiation and growth criteria. The most common form for such criteria is the requirement that the crack must grow in such a way that some parameter (e.g. the dynamic stress intensity factor, K_I^d) defined as part of the crack-tip field maintains a value that is specific to the material. This value, representing the resistance of the material to the advance of the crack, is called the dynamic fracture

toughness (K_{IC}^d) of the material, and it can be determined through experimental measurements only. Thus, in its most general form this can be represented as

$$K_I^d[l(t), v(t), P(t), t] = K_{IC}^d[v(t), \ldots] \qquad (39)$$

where the left hand side is the solution obtained from elasticity and the right hand side represents the material property determined experimentally. Here l, v and P are the instantaneous crack length, crack speed and applied load respectively. Equation (39) is a complete statement of a crack growth criterion whose solution provides an equation of motion for the crack tip under appropriate initial conditions [22,23]. We will first consider the characteristics of the left hand side of Eq. (39).

2.4.1 Dynamic Stress Intensity Factor, K_I^d. The physical problem at hand involves transient loading of the existing fractures in the damage mechanics framework. Several authors have studied the problem of transient loading of a crack using analytical and numerical techniques [22–43]. The stress intensity factor for transient loading of cracks, referred to as the dynamic stress intensity factor, K_I^d (see left hand side of Eq. (39)), has two important general characteristics:

(1) For a stationary finite crack ($dl/dt \equiv v = 0$) under transient loading conditions, K_I^d evolves with time following the application of loads. It rises sharply with time, overshoots the equivalent quasi-static value K_{st} by a considerable amount, and then oscillates around the static value with decreasing amplitude. This oscillation is due to the Rayleigh waves traveling back and forth along the surface of the crack with decreasing intensity (for, e.g., see Refs. [22,23]). This generalized behavior can be summarized by the relationship

$$\frac{K_I^d(t)}{K^{st}} = \Lambda\left(\frac{c_R t}{b}\right) \qquad (40)$$

where Λ is a function of a dimensionless, crack-length-related time $c_R t/b$, describing the oscillation of $K_I^d(t)$ around its quasi-static value, K^{st}. Here, c_R is the Rayleigh wave speed of the material and b is the half-length of the crack. After an early steep increase, Λ reaches a maximum value (up to about 30% more than its quasi-static value), then oscillates around the value 1 with diminishing amplitude, becoming equal to the average value of 1 for longer times. The increase in Λ, before the arrival of reflections, is known analytically [34] and is given by

$$\frac{K_I^d(t)}{K^{st}} = \sqrt{\frac{c_p t}{b}} \qquad (41)$$

where c_p is the dilatational or the P-wave speed of the medium. This initial increase and subsequent oscillations can be approximated as

$$\Lambda\left(\frac{c_R t}{b}\right) \approx 1 - e^{(c_R t/2b)} J_0(4c_R t/b) \qquad (42)$$

where $J_0(x)$ is the zeroth order Bessel function.

We ignore this effect since our crack sizes are much smaller than any model dimension. This means that any numerical computation will have to be temporally resolved to capture this transient effect occurring at time scales much smaller than the time scale associated with the larger model itself making the problem computationally expensive.

(2) For a dynamically growing crack tip ($dl/dt \equiv v \neq 0$), a second key result was obtained by Ref. [29] who showed that for an unbounded body subjected to time independent load-

ing, the dynamic stress intensity factor at the running crack-tip can be expressed as a universal function of instantaneous crack-tip speed, $v(t)$, multiplied by the equilibrium stress intensity factor for the given applied loading and the instantaneous amount of crack growth, i.e.,

$$K_I^d[v(t)] = k[v(t)]K_I[l(t)] \; ; \; k(v) \approx \frac{(1 - v/c_R)}{\sqrt{1 - v/c_p}} \qquad (43)$$

While this result holds only for a single crack under conditions described above, we nevertheless invoke it as an approximation to obtain the dynamic stress intensity factor of the micro-cracks in our model. We will now examine the right hand side of Eq. (39) which represents the fracture toughness of the material.

2.4.2 Dynamic Initiation Toughness. As a material parameter the fracture toughness, K_{IC} (for quasi-static loading), K_{IC}^D (for dynamic initiation) and K_{IC}^d (for dynamic propagation) can only be obtained through experimental measurements and is found to vary with loading rate. Under impact loading conditions, high loading rates occur at the pre-existing crack-tip. A parameter $\dot{K}_I$ characterizing the loading rate is defined as

$$\dot{K}_I = \frac{K_{IC}}{t_C} \qquad (44)$$

where K_{IC} is the mode-I critical stress intensity factor at the instant of crack initiation (fracture toughness) and t_C denotes the time from the beginning of loading to the instant at which fracture initiation occurs. Usually, the crack-tip loading rates range from $\dot{K}_I \sim \text{MPa}\sqrt{\text{ms}^{-1}}$ for quasi-static loading to as high as $\dot{K}_I \sim 10^8 \text{MPa}\sqrt{\text{ms}^{-1}}$ for impact loading.

One can view the initiation of a stationary crack as a process where the defects in the vicinity of the crack tip develop into small secondary cracks, and these secondary cracks coalesce with the original crack so as to enlarge it further. The formation of the secondary cracks in the vicinity of the crack tip is controlled by the stress level at that location. This process is also closely connected to how the stress level reaches the critical value, i.e., the loading history at the location of the defects. The authors of Ref. [37] studied this problem of fracture initiation at the tip of a crack in terms of activating a single flaw at some distance away from the tip of a semi-infinite crack in an unbounded two-dimensional solid subjected to spatially uniform but temporally varying crack-face pressure. Fracture initiation was assumed to be synonymous with attaining a critical stress at the fracture site. Their results agreed well with typical experimental data of dynamic crack initiation in nominally brittle solids. Thus, due to material inertia a solid may exhibit totally different fracture initiation resistance (initiation toughness) from those under quasi-static loading conditions [44,45]. This, according to Ref. [37], is related to the finite time it takes to establish a sizable region of K_I field dominance at the vicinity of the main crack tip. This material property, that depends on the loading rate, is thus called the *Dynamic Initiation Toughness*, K_{IC}^D, and its quasi-static limit is K_{IC}^{SS}. This can be represented as $K_{IC}^D = f(\dot{K}_I)K_{IC}^{SS}$ where $f(\dot{K}_I) (\geq 1)$ takes into account the increased initiation toughness due to loading rate (Fig. 2). Since this is a inertia dominated phenomenon, for this work we assume the following functional form for $f_D(\dot{K}_I)$ that best fits the data (as shown by the dashed line in Fig. 2)

$$f_D(\dot{K}_I) = 1 + \left(\frac{\dot{K}_I}{K_{IC}^{SS}}\right) \times 2 \times 10^{-5} \qquad (45)$$

2.4.3 Dynamic Propagation Toughness. Once the crack-tip starts propagating, the material resistance ahead of the crack-tip has been shown to depend on the crack-tip speed [43,44]. This
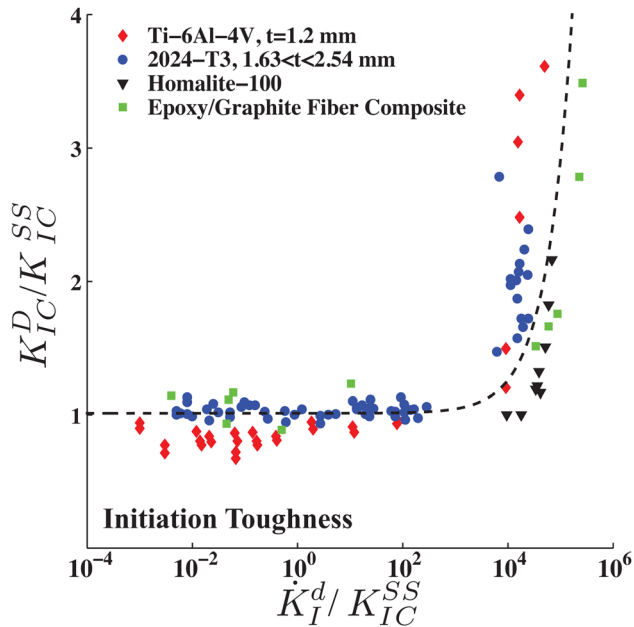
Fig. 2 (*a*) Normalized dynamic initiation toughness K_{IC}^D for fracture initiation as a function of loading rate for several materials (from Ref. [48])

Fig. 3 Normalized dynamic propagation toughness K_{IC}^d for fracture propagation as a function of crack-tip velocity for various materials (from Ref. [48])

crack-speed dependent resistance is called *Dynamic Propagation Toughness,* $K_{IC}^d(v)$ and has been discussed earlier as the right hand side of Eq. (39); Refs. [44,45] explain this in terms of the interplay of nonlinear and inertial effects associated with the propagating crack-tip. This effect of increasing fracture resistance with speed was demonstrated numerically by Ref. [46] for Mode-III crack growth and by Ref. [47] for Mode-I crack growth under plane stress conditions in an elastic-perfectly plastic material by means of small scale yielding calculations. They showed that as the crack speed was increased, the interaction of inertia and local near tip nonlinearities necessitated the monotonic increase of $K_{IC}^d(v)$ in order to keep satisfying a local critical crack opening displacement criterion.

Beyond a critical crack speed further increase in $K_{IC}^d(v)$ becomes energetically unfavorable and the single initial crack prefers to branch into one or more cracks; each of these cracks in turn follow the same crack growth resistance criteria. This limiting speed is called the branching speed, v_m. This speed varies from material to material and decreases with increasing material ductility. For, e.g., 2024-T3 Aluminum $v_m \approx 0.03c_R$, for 4340 steel $v_m \approx 0.32c_R$ and for Glass $v_m \approx 0.55c_R$. These experimental observations have been summarized in Fig (3). We represent this with the following functional form,

$$K_{IC}^d(v) = K_{IC}^{SS}\left\{\frac{1 + (v/v_m)^5}{\sqrt{1 - v/c_p}}\right\} \qquad (46)$$

2.4.4 Crack-Tip Equation of Motion. Based on the experimental observations discussed above whose most important implication is that for either initiation or propagation, very similar trends are observed regardless of material, and we are now in a position to write an expression that describes both the initiation and growth of fractures at high loading rates.

Initiation Criterion: The crack will initiate motion when

$$K_I^d(v = 0, \dot{K}_I) = K_{IC}^D(\dot{K}_I) \qquad (47)$$

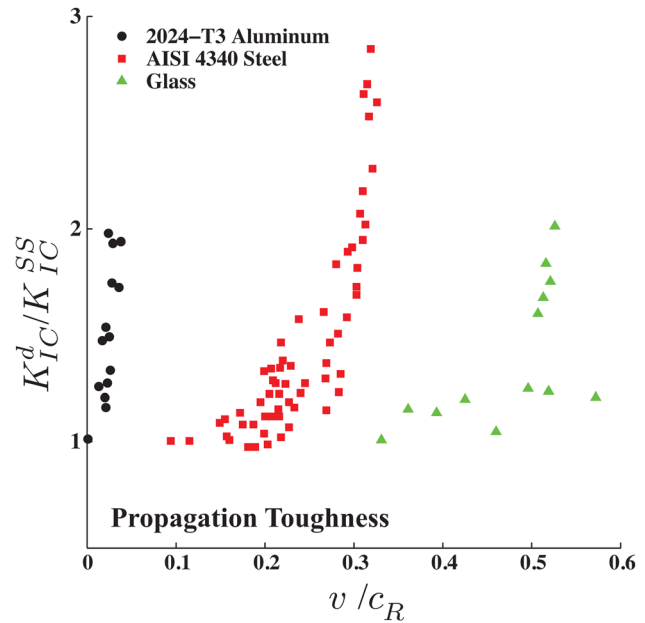where K_I is the stress intensity factor from Eqs. (14) or (17) depending on the remote loading regime.

Growth Criterion:
During the process of crack growth, if small scale yielding conditions prevail, the fracture criterion stipulates:

$$K_I^d(t) = K_I^d[l(t), v(t), P(t), t] = K_{IC}^d(v) \qquad (48)$$

where the left-hand side is the dynamic stress intensity factor or otherwise known as the "driving force," which in principle is entirely determined through an analysis of a boundary/initial value problem. The right-hand side represents the material "resistance" to dynamic fracture at various speeds, called the dynamic fracture toughness which can only be determined through experiments. The above equation is in general a first order nonlinear differential equation for $l(t)$ and provides the evolution equation for crack growth, i.e., a crack-tip equation of motion. For the specific problem at hand, the dynamic stress intensity factor for the propagating crack is given by

$$K_I^d(t) = k(v)K_I \quad \text{where} \quad k(v) \approx \frac{(1 - v/c_R)}{\sqrt{1 - v/c_p}} \qquad (49)$$

where K_I is the quasi-static stress intensity factor of an equivalent crack of the same length but growing at zero speed. It is obtained from Eqs. (14) or (17) depending on the remote loading regime. Combining Eqs. (46), (48) and (49), we obtain a nonlinear equation for crack-tip speed as,

$$\frac{K_I(1 - v/c_R)}{\sqrt{1 - v/c_p}} = K_{IC}^{SS}\left\{\frac{1 + (v/v_m)^5}{\sqrt{1 - v/c_p}}\right\} \qquad (50)$$

This expression is solved to obtain the crack speed which is then used in Eq. (38) to complete the damage evolution equation.

3 Results and Discussion

3.1 Experimental Results and Observations for Dionysus-Pentelicon Marble. The authors of Ref. [48] have conducted uniaxial experiments, over a wide range of strain-rates, on Dionysus-Pentelicon marble which is a high quality white marble
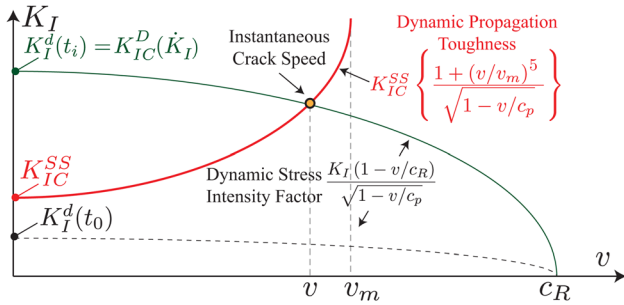
Fig. 4 Graphical representation of the solution to Eq. (50)

Fig. 6 Stress-strain curves for marble under compressive loading at strain rates differing by more than eight orders of magnitude (from Ref. [48])

that was originally used in the construction of the classical Parthenon. Low strain-rate experiments ($\dot{\varepsilon} \sim 10^{-6} - 10^{-3}$) were conducted using a conventional load frame apparatus whereas high strain-rate experiments ($\dot{\varepsilon} \sim 10^2 - 10^3$) were conducted using split Hopkinson bar technique. In addition to these fracture and fragmentation studies were conducted using high-speed photography in conjunction with a variety of interferometric techniques. The marble is composed of approximately 98% calcite with less than 1% quartz. This marble has a density of 2750 kg/m^3, Young's Modulus of 78 GPa and its Poisson's ratio is 0.31. Figure 5 shows optical micrographs of the marble specimens used in the experiments. The average size of these grains were measured and found to be 400 μm in each orientation with the largest grains having dimensions of ~1 mm.

The authors of Ref. [48] observed extreme strain-rate sensitivity in the dynamic uniaxial compressive loading of marble (see Fig. 6). The compressive strength was found to increase by a factor of 7 when strain rate was increased from the quasi-static regime to the regime corresponding to impact and explosive loading. Unexpectedly high crack-tip speeds during dynamic crack growth in marble. In certain orientations maximum speeds reached and even exceeded the Rayleigh wave speed. Failure involved complex crack-tip branching phenomena as well as dynamic coalescence of multiple micro-cracks with the dominant cracks.

3.2 Model Parameters. We now we will use the parameters from the experiments described above to test the constitutive model developed in the previous section. We set the size of our penny crack, $a = 1$mm and we assume the friction coefficient between the faces of the penny crack is $f = 0.7$. Following Ref. [12], we determine the initial damage, D_0 and hence the flaw density N_V, from the quasi-static stress-strain curve for marble (Fig. 6). This involves solving for the value of D (in the uniaxial version of the stress-strain curve in Eq. (23)) corresponding to the lowest nonlinear stress value from the experiments. By this
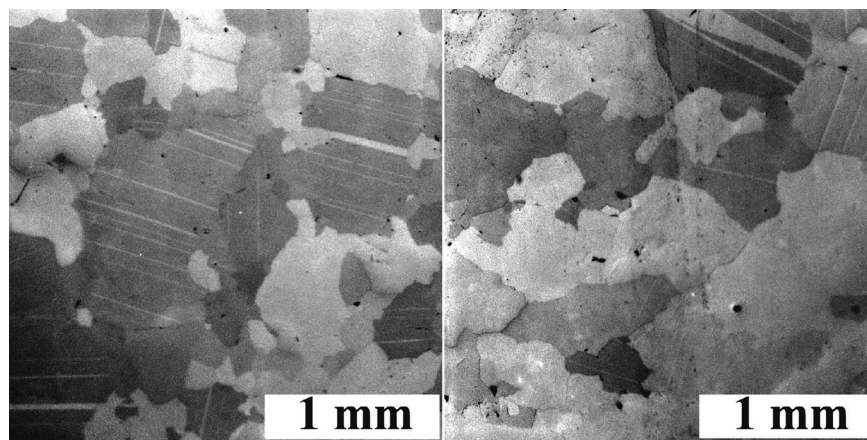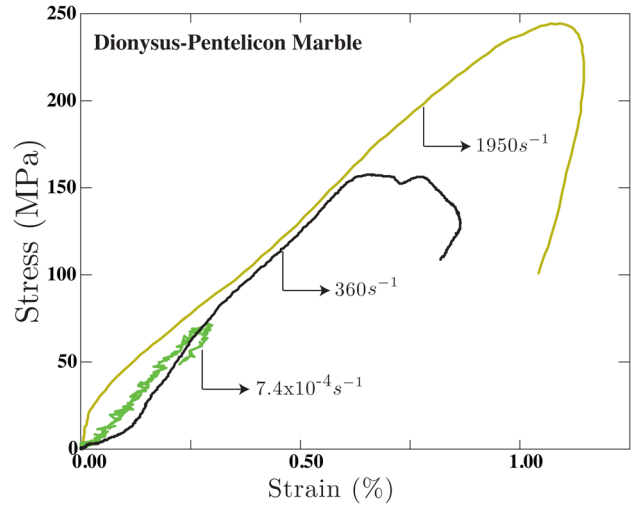
method we obtain $D_0 = 0.1$. The only remaining parameter is the branching speed v_m and we assume this to be equal to $0.35c_R$ since no detailed experimental results exist. This is a mean branching speed for brittle materials that have some amount of ductility.

3.3 Numerical Implementation and Convergence Studies. A constitutive time-integration procedure for the model described in the previous section has been implemented in the finite element program ABAQUS-Explicit by writing a USER MATERIAL (VUMAT) subroutine. Integration of the damage evolution equation (Eq. (38)) is carried out using a fifth order Runge-Kutta scheme with adaptive step-size control [49]. The crack-tip equation of motion (Eq. (50)) is solved using the bisection method. The continuum constitutive law developed in the previous section contains no direct length scale. The micromechanical definition of the scalar damage parameter involves a length scale, the size of the penny crack a. However, in the continuum form of the constitutive law it is simply a scalar dimensionless state variable that determines the evolution of the modulus tensor and the stress-strain relationship. However, the damage evolution law, Eq. (38), depends on the size of the penny crack a. We thus use this length-scale to discretize our model. For computational ease we conducted axisymmetric calculations on a cylindrical specimen of radius, $R = 6$ mm and height, $H = 10$ mm. A constant velocity, V, boundary condition was applied on one end

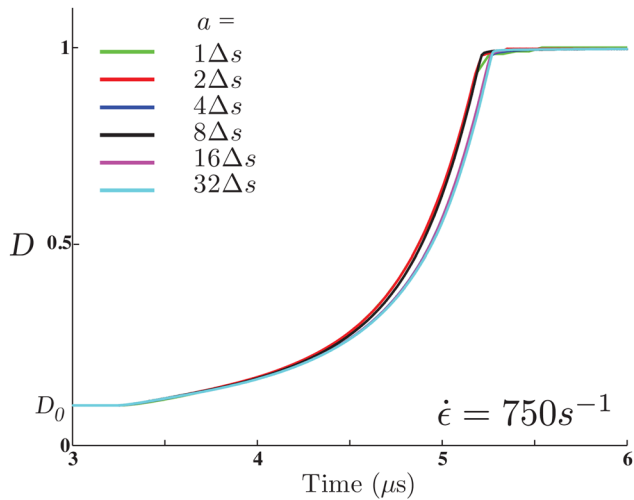**Fig. 5 Optical micrographs of the Dionysus-Pentelicon marble**

Fig. 7 Effect of grid resolution on the temporal evolution of the scalar damage parameter, D. Here Δs is the size of the finite element and a is the size of the penny crack.

Fig. 9 Numerically obtained stress-strain curves at different strain-rates for marble based on the constitutive model developed
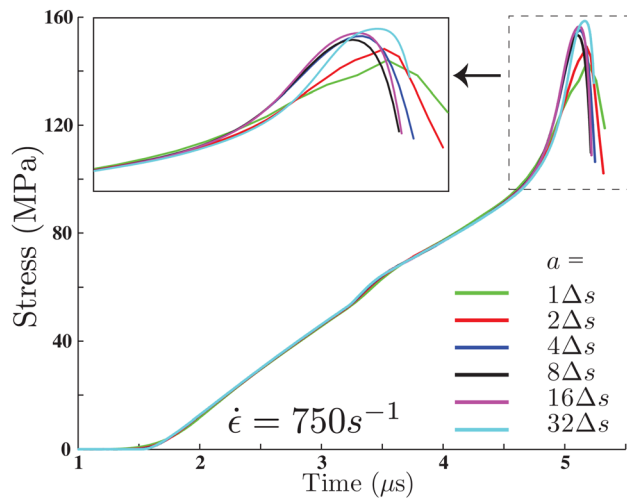

Fig. 8 Effect of grid resolution on the temporal evolution of uniaxial stress. Here Δs is the size of the finite element and a is the size of the penny crack.

of the specimen. The average applied strain rate is then given by $\dot{\varepsilon} = V/H$. As one can see from Figs. 7 and 8, the numerical scheme does indeed converge for the evolution of damage, D and for the most part of stress evolution. Instabilities develop when the material reaches its peak failure strength and begins to soften. These instabilities develop at values of $D < 1$ and correspond to the loss of ellipticity in the constitutive description. We plan to carefully study the onset of these instabilities and their effect of the bulk response of the material in the future.

3.4 Comparison With Experimental Results. We again conducted axisymmetric calculations on a cylindrical specimen of radius, $R = 6$ mm and height, $H = 10$ mm as used by Ref. [48] in their high-strain rate experiments. A constant velocity, V, boundary condition was applied on one end of the specimen. The average applied strain rate is then given by $\dot{\varepsilon} = V/H$.

We conducted numerical experiments for strain-rates ranging from 1 s^{-1} to 5000 s^{-1}. We chose an element size Δs such that $a = 10\Delta s$. Since an explicit time-integration procedure was used, we limited ourselves to high-strain rate experiments. The uniaxial stress-strain curves are shown in Fig. 9. The results are shown only up to peak failure strength. The strong strain-rate sensitivity
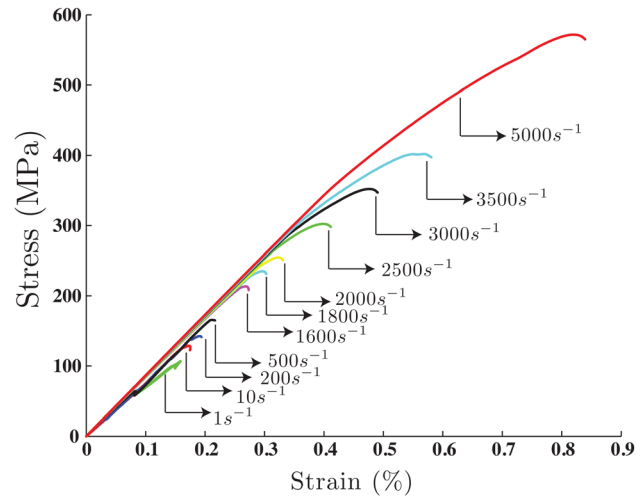
of the constitutive law is apparent in this figure. This rate dependence is a direct consequence of dynamic initiation and propagation criteria for the micro-cracks. The evolution of the scalar damage variable, D, depends not only on the micro-crack tip stress field but also the time rate of this field. The rate sensitivity for the micro-crack directly translates to strain-rate sensitivity of the continuum constitutive law.

Another interesting feature that manifests uniquely, due to the crack growth law incorporated in this work, is the evolution of the scalar damage parameter D, at various strain rates, as seen in Figs. 10 and 11 . As we can see from the insets $Z1$ and $Z2$ in Fig. (10), the damage evolution is delayed but still quite rapid and D jumps quite dramatically over a few microseconds. This physically means that even if the loading rate is relatively slow the onset of failure could still be quite sudden due to rapid acceleration of the micro-cracks leading to the fast evolution of D. For the case of $\dot{\varepsilon} = 10s^{-1}$, we see a slow evolution of D from $t \sim 100 \text{ } \mu$s to $t \sim 160 \text{ } \mu$s followed by a rapid evolution over a few μs. The slow evolution phase corresponds to micro-crack loading being just large enough to barely violate the crack growth resistance criterion resulting in small values of crack speeds that translate to the slow evolution phase of D. Physically, this could be interpreted as "acoustic emission" signatures that are experimentally
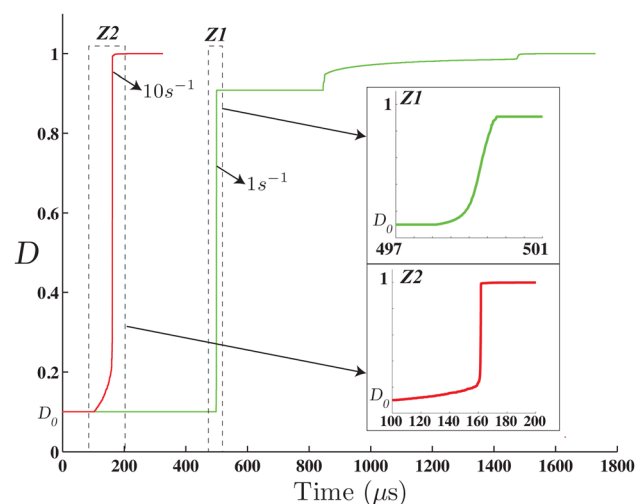

Fig. 10 Temporal evolution of the scalar damage parameter D for lower strain rate simulations ($\dot{\varepsilon} = 1s^{-1}$ and $10 \text{ } s^{-1}$)
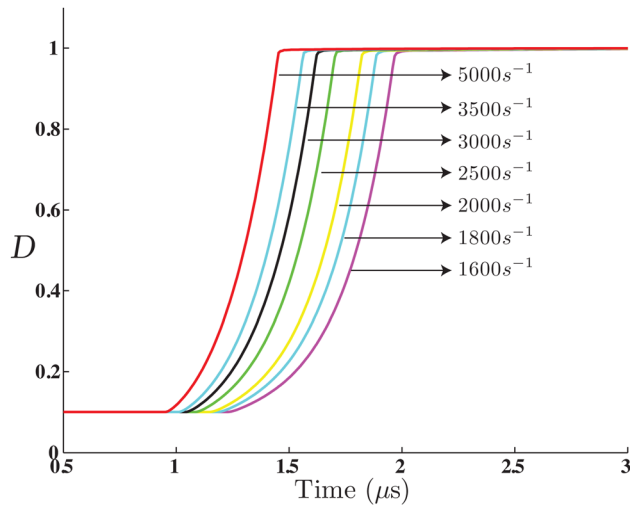
Fig. 11 Temporal evolution of the scalar damage parameter D for higher strain rate simulations ($\dot{\varepsilon} = 1600s^{-1}$ to $5000 \ s^{-1}$)

Fig. 12 Variation of peak or failure stress with strain rate. Experimental results are compared with numerical simulations.

observed to increase prior to the onset of failure. For higher loading rates, D attains its maximum value over a period of 0.5 to 1.0 μs signaling a rapid failure event (Fig. 11). As expected damage evolution occurs earlier and in a shorter period of time as the loading rate increases.

Finally, we would like to compare our results with the experiments, conducted by Ref. [48], described earlier in the paper. We do not directly compare the stress-strain curves as the amount of strain predicted by our constitutive law is about a factor of 2-3 smaller than that measured in the experiments. We suspect this is because we do not take into account any plastic deformation of the calcite grains in the constitutive description. We plan to rectify this in the future. We thus plan instead to compare the peak stress at failure under uniaxial compression. Since this data exists in Ref. [48] for a wide range of strain-rate ($\dot{\varepsilon} \sim 10^{-6}s^{-1}$ to $10^3 s^{-1}$) we consider this as the best metric for comparison of the constitutive law over a wide range of strain-rates. These results are summarized in Fig. 12. Our model predictions are a very good fit to the experimental data for strain rates ranging from $1 \ s^{-1}$ to 5000 s^{-1}. Our success in predicting the increase in strength with loading rate clearly related to the proper modeling of crack growth dynamics.

We would like to emphasize that in obtaining this fit we only needed the elastic constants (determined experimentally), penny
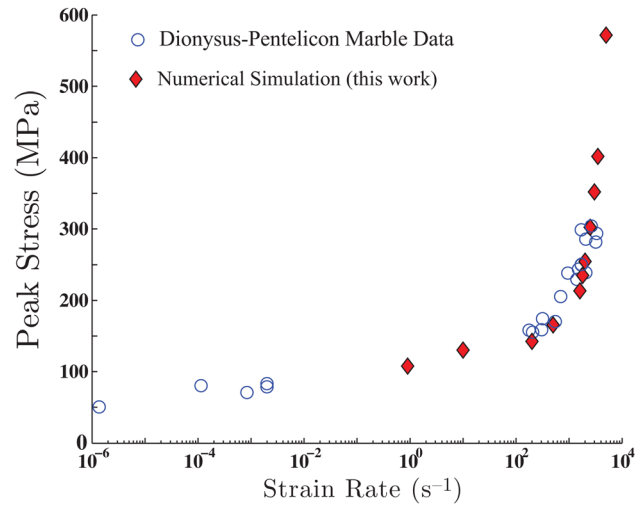
crack size (estimated to be of the order of measured average grain size), initial damage D_0 (estimated from the quasi-static stress-strain curve) and the branching speed (approximated to be $0.35c_R$).

4 Dynamic Earthquake Rupture Application

One of the important questions in earthquake source physics is to understand the effect of dynamic earth-quake ruptures and the associated high loading-rate effects in the generation of new damage, in the medium hosting earthquake faults, and, at the same time, to explore the effect of damage generation on the rupture propagation. Specifically, some of these questions are: (1) What is the spatial extent of a dynamically generated off-fault damage? (2) How is a propagating rupture affected by pre-existing off-fault damage? (3) How does the off-fault damage contribute to asymmetric rupture propagation?

The constitutive model we have developed can now be used to address these questions. To that end, we simulate an earthquake rupture as a dynamic Model-II rupture propagating along an interface that has damaged rock, following the constitutive law developed here, on one side and an undamaged rock following linear elastic constitutive law on the other side. The interfacial strength is governed by a linear slip-weakening law as shown in Fig. 13. We use the elastic constants of granite ($E = 75$ GPa, $\nu = 0.25$). The
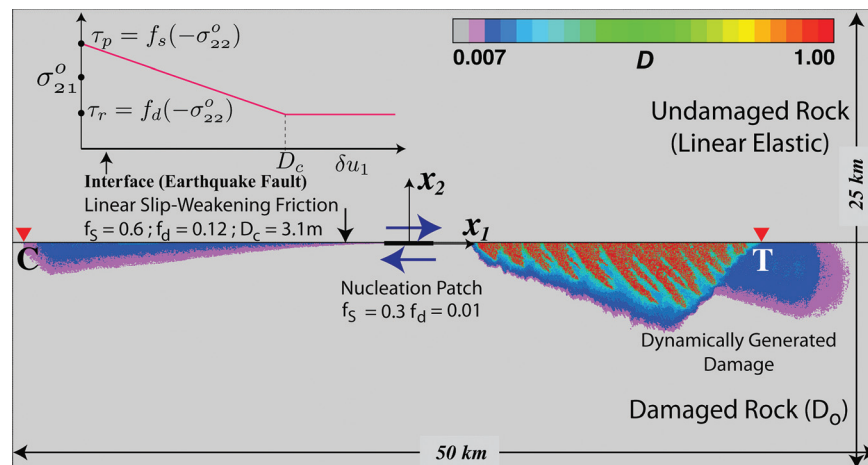

Fig. 13 Snapshot of a bilateral rupture propagating on the boundary between damaged and undamaged rock. Note the generation of dynamic damage in the tensile lobe of the right rupture tip. Rupture tips are denoted by the inverted triangles.

initial flaw size was assumed to be 25 m corresponding to large scale damage influenced by the medium from previous earthquake events and initial damage, D_0, was set to be 0.007. Branching speed v_m was assumed to be $0.35c_R$. To speed up the computation we set the element size to be the same as the flaw size. The process zone size (or equivalently the cohesive zone size) at zero rupture speed for the assumed friction law parameters is 2 km.

Figure 13 shows a snapshot of bilateral rupture propagating along the interface between an undamaged material above and a damaged material below. Since the rupture is right-lateral, the tip propagating to the left puts the damaged material in compression (which we define as the C direction) while the tip propagating to the right puts the damaged material in tension (the T direction). Note that most of the new damage is generated in the tensile lobe of the tip propagating to the right and, as expected, the tip traveling in the T direction is slower than that traveling in the P direction. In addition, we observe the formation of localized damage zones that could mature ultimately into branched faults. We would like to note that we have not fully explored the localization phenomenon and at this stage do not have an insight on mesh dependence. We plan to conduct detailed studies of this phenomenon in the future.

5 Summary

We have developed a micro-mechanically motivated constitutive law that is an extension of [2,12]. A unique feature of this new constitutive law is the incorporation of crack growth dynamics that is consistent with recent theoretical and experimental studies of high-speed crack propagation. The resultant crack growth law relates the crack speed to the instantaneous value of the stresses at the crack tip and also their time rates. This translates directly (and naturally) into strain-rate sensitivity in the constitutive description.

The constitutive model was tested by predicting experiments on Dionysus-Pentelicon marble [48]. All the parameters of the model were experimentally derived or inferred from quasi-static data. These parameters were then used to predict the failure strength at higher loading rates. We have shown that incorporation of proper crack growth dynamics is the key to correctly represent brittle failure over a wide range of loading rates.

References

[1] Budiansky, B., and O'Connell, R. J., 1976, "Elastic Moduli of a Cracked Solid," Int. J. Solids Struct., **12**(2), pp. 81–97.
[2] Deshpande, V. S., and Evans, A. G., 2008, "Inelastic Deformation and Energy Dissipation in Ceramics: A Mechanism-Based Constitutive Model," J. Mech. Phys. Solids, **56**(10), pp. 3077–3100.
[3] Kachanov, M. L., 1982, "A Micro-Crack Model of rock Inelasticity Part I: Frictional Sliding on Micro-Cracks," Mech. Mater., **1**(1), pp. 19–27.
[4] Kachanov, M. L., 1982, "A Micro-Crack Model of Rock Inelasticity Part II: Propagation of Micro-Cracks," Mech. Mater., **1**(1), pp. 19–27.
[5] Kachanov, M. L., 1987, "Elastic Solids with Many Cracks: A Simple Method of Analysis," Int. J. Solids Struct., **23**(1), pp. 23–43.
[6] Sayers, C. M., and Kachanov, M. L., 1995, "Microcrack-Induced Elastic Wave Anisotropy of Brittle Rocks," J. Geophys. Res., **100**, pp. 4149–4149.
[7] Krajcinovic, D., 1996, *Damage Mechanics*, Elsevier, Amsterdam.
[8] Sevostianov, I., and Kachanov, M., 2002, "On Elastic Compliances of Irregularly Shaped Cracks," Int. J. Fract., **114**(3), pp. 245–257.
[9] Paliwal, B., and Ramesh, K. T., 2008, "An Interacting Micro-Crack Damage Model for Failure of Brittle Materials Under Compression," J. Mech. Phys. Solids, **56**(3), pp. 896–923.
[10] Charles, R. J., 1958, "Dynamic Fatigue of Glass," J. Appl. Phys., **29**(12), pp. 1657–1662.
[11] Maugis, D., 1985, "Subcritical Crack Growth, Surface Energy, Fracture Toughness, Stick-Slip and Embrittlement," J. Mater. Sci., **20**(9), pp. 3041–3073.
[12] Ashby, M. F., and Sammis, C. G., 1990, "The Damage Mechanics of Brittle Solids in Compression," Pure Appl. Geophys., **133**(3), pp. 489–521.
[13] Bhat, H. S., Sammis, C. G., and Rosakis, A. J., 2011, "The Micromechanics of Westerley Granite at Large Compressive Loads," Pure Appl. Geophys., **168**(12), pp. 1–18.
[14] Nemat-Nasser, S., and Horii, H., 1982, "Compression-Induced Non-Planar Crack Extension with Application to Splitting, Exfoliation, and Rockburst," J. Geophys. Res., **87**(B8), pp. 6805–6821.
[15] Ashby, M., and Hallam Née Cooksley, S. D., 1986, "The Failure of Brittle Solids Containing Small Cracks Under Compressive Stress States," Acta Metall. Mater., **34**(3), pp. 497–510.
[16] Jeyakumaran, M., and Rudnicki, J. W., 1995, "The Sliding Wing Crack—Again!," Geophys. Res. Lett., **22**(21), pp. 2901–2904.
[17] Kranz, R. L., 1983, "Microcracks in Rocks: A Review," Tectonophysics, **100**(1–3), pp. 449–480.
[18] Hill, R., and Rice, J. R., 1973, "Elastic Potentials and the Structure of Inelastic Constitutive Laws," SIAM J. Appl. Math., **25**(3), pp. 448–461.
[19] Rice, J. R., 1975, "Continuum Mechanics and Thermodynamics of Plasticity in Relation to Microscale Deformation Mechanisms," *Constitutive Equations in Plasticity*, A. S. Argon, ed., MIT Press, Cambridge, MA.
[20] Drucker, D. C., and Prager, W., 1952, "Soil Mechanics and Plastic Analysis or Limit Design," Q. Appl. Math., **10**(2), pp. 157–165.
[21] Bristow, J. R., 1960, "Micro-Cracks, and the Static and Dynamic Elastic Constants of Annealed and Heavily Cold-Worked Metals," Br. J. Appl. Phys., **11**, pp. 81–85.
[22] Freund, L. B., 1990, *Dynamic Fracture Mechanics*, Cambridge University Press, Cambridge.
[23] Broberg, K. B., 1999, *Cracks and Fracture*, Academic Press, New York.
[24] Achenbach, J., 1970, "Extension of a Crack by a Shear Wave,"Z. Angew. Math. Phys., **21**(6), pp. 887–900.
[25] Baker, B., 1962, "Dynamic Stresses Created by a Moving Crack," J. Appl. Mech., **29**(3), pp. 449–458.
[26] Brock, L. M., 1991, "Exact Transient Results for Penny-Shaped Crack Growth under Combined Loading," Int. J.Solids Struct., **28**(4), pp. 517–531.
[27] Freund, L. B., 1972, "Crack Propagation in an Elastic Solid Subjected to General Loading-I. Constant Rate of Extension," J. Mech. Phys. Solids, **20**(3), pp. 129–140.
[28] Freund, L. B., 1972, "Crack Propagation in an Elastic Solid Subjected to General Loading-ii. Non-Uniform Rate of Extension," J. Mech. Phys. Solids, **20**(3), pp. 141–152.
[29] Freund, L. B., 1973, "Crack Propagation in an Elastic Solid Subjected to General Loading-iii. Stress Wave Loading," J. Mech. Phys. Solids, **21**, pp. 47–61.
[30] Freund, L. B., 1974, "Crack Propagation in an Elastic Solid Subjected to General Loading.-iv. Obliquely Incident Stress Pulse," J. Mech. Phys. Solids, **22**, pp. 137–146.
[31] Gross, D., and Seelig, T., 2006, *Fracture Mechanics: With an Introduction to Micromechanics*, Springer-Verlag, Berlin.
[32] Kalthoff, J. F., and Shockey, D. A., 1977, "Instability of Cracks Under Impulse Loads," J. Appl. Phys., **48**, pp. 986–993.
[33] Kim, K. S., 1979, "Dynamic Propagation of a Finite Crack," Int. J. Solids Struct., **15**, pp. 685–699.
[34] Kostrov, B. V., 1974, "Crack Propagation at Variable Velocity," Prikl. Mat. Mekh., **38**, pp. 511–519.
[35] Kostrov, B. V., 1984, "On the Crack Propagation with Variable Velocity," Int. J. Fract., **26**(4), pp. 370–379.
[36] Liu, C., and Rosakis, A. J., 1994, "Investigation of Transient Effects for Dynamically Initiating and Growing Cracks Under Stress Wave Loading Conditions," *Dynamic Fracture Mechanics,* M. H. Aliabadi, ed., Computational Mechanics Publication, Southhampton, UK, Chap. 4.
[37] Liu, C., Knauss, W. G., and Rosakis, A. J., 1998, "Loading Rates and the Dynamic Initiation Toughness in Brittle Solids," Int. J. Fract., **90**(1), pp. 103–118.
[38] Owen, D. M., Zhuang, S., Rosakis, A. J., and Ravichandran, G., 1998, "Experimental Determination of Dynamic Crack Initiation and Propagation Fracture Toughness in Thin Aluminum Sheets," Int. J. Fract., **90**(1), pp. 153–174.
[39] Ravera, R. J., and Sih, G., 1970, "Transient Analysis of Stress Waves Around Cracks under Anti-Plane Strain," J. Acoust. Soc. Am., **47**, pp. 875–881.
[40] Shockey, D. A., Kalthoff, J. F., and Erlich, D. C., 1983, "Evaluation of Dynamic Crack Instability Criteria," Int. J. Fract., **22**(3), pp. 217–229.
[41] Sih, G. C., 1968, "Some Elastodynamic Problems of Cracks," Int. J. Fract., **4**(1), pp. 51–68.
[42] Sih, G. C., Embley, G. T., and Ravera, R. S., 1972, "Impact Response of a Finite Crack in Plane Extension," Int. J. Solids Struct., **8**(12), pp. 977–993.
[43] Zehnder, A. T., and Rosakis, A. J., 1990, "Dynamic Fracture Initiation and Propagation in 4340 Steel under Impact Loading," Int. J. Fract., **43**(4), pp. 271–285.

[44] Rosakis, A. J., Duffy, J., and Freund, L. B., 1984, "The Determination of Dynamic Fracture Toughness of Aisi 4340 Steel by the Shadow Spot Method," J. Mech. Phys. Solids, **32**(6), pp. 443–460.

[45] Rosakis, A., and Zehnder, A., 1985, "On the Dynamic Fracture of Structural Metals," Int. J. Fract., **27**(3), pp. 169–186.

[46] Freund, L. B., and Douglas, A. S., 1982, "The Influence of Inertia on Elastic-Plastic Anti-Plane-Shear Crack Growth," J. Mech. Phys. Solids, **30**(1/2), pp. 59–74.

[47] Deng, X., and Rosakis, A. J., 1991, "Dynamic Crack Propagation in Elastic-Perfectly Plastic Solids under Plane Stress Conditions," J. Mech. Phys. Solids, **39**(5), pp. 683–722.

[48] Rosakis, A. J., 1999, "Explosion at the Parthenon: Can We Pick Up the Pieces?," Technical Report No. GALCIT SM REPORT 99-3.

[49] Press, W. H., Teukolsky, S. A., Vetterling, W. T., and Flannery, B. P., 1993, *Numerical Recipes in Fortran 77: The Art of Scientific Computing 1*, Cambridge University Press, Cambridge.